Swift heavy ion irradiation of Cu–Zn–Al and Cu–Al–Ni alloys

2009 J. Phys.: Condens. Matter 21 185009

(http://iopscience.iop.org/0953-8984/21/18/185009)

J. Phys.: Condens. Matter **21** (2009) 185009 (8pp) doi:10.1088/0953-8984/21/18/185009

Swift heavy ion irradiation of Cu–Zn–Al and Cu–Al–Ni alloys

E Zelaya[1,2], A Tolley[2,3], A M Condo[2,3] and G Schumacher[4]

[1] Electron Microscopy for Materials Research, University of Antwerp, Groenenborgerlaan 171, B-2020 Antwerp, Belgium
[2] Consejo Nacional de Investigaciones Cientificas y Tecnicas, Argentina
[3] Centro Atómico Bariloche, CNEA, Avenida Bustillo 9500, 8400 San Carlos de Bariloche, Argentina
[4] Hahn-Meitner-Institut Berlin, Glienicker Straße 100, 14109 Berlin, Germany

Received 7 November 2008, in final form 23 February 2009
Published 24 March 2009
Online at stacks.iop.org/JPhysCM/21/185009

Abstract
The effects produced by swift heavy ions in the martensitic (18R) and austenitic phase (β) of Cu based shape memory alloys were characterized. Single crystal samples with a surface normal close to $[210]_{18R}$ and $[001]_{\beta}$ were irradiated with 200 MeV of Kr^{15+}, 230 MeV of Xe^{15+}, 350 and 600 MeV of Au^{26+} and Au^{29+}. Changes in the microstructure were studied with transmission electron microscopy (TEM) and high resolution transmission electron microscopy (HRTEM). It was found that swift heavy ion irradiation induced nanometer sized defects in the 18R martensitic phase. In contrast, a hexagonal close-packed phase formed on the irradiated surface of β phase samples. HRTEM images of the nanometer sized defects observed in the 18R martensitic phase were compared with computer simulated images in order to interpret the origin of the observed contrast. The best agreement was obtained when the defects were assumed to consist of local composition modulations.

1. Introduction

The special properties of shape memory alloys are due to the diffusionless martensitic transformation. Cu–Zn–Al and Cu–Al–Ni alloys exhibit a martensitic transformation from the high temperature β phase, with a cubic structure, to the 18R martensitic phase, with a monoclinic structure, at lower temperature [1]. The martensitic transformation temperature is strongly composition dependent. Therefore, it is possible to obtain the β phase or the 18R martensitic phase at room temperature by choosing the appropriate composition. However, the transformation temperature is also sensitive to order degree, defects and precipitates [2].

Some irradiation processes are an effective method to induce structural or microstructural changes in Cu based shape memory alloys. In Cu–Zn–Al alloys, irradiation experiments with electrons or low energy ions have been carried out in which the main energy deposition mechanism was that of elastic collisions with the nuclei. Irradiation experiments with 2.65 MeV electrons [3] or with 2 MeV protons [4] in the martensitic phase were found to induce the stabilization of this phase, that is, to shift the martensitic transformation temperature to higher values. Instead, electron irradiation experiments in the high temperature β phase did not modify the martensitic transformation temperature [3]. However, irradiation experiments with 170 and 300 keV Cu ions in the β phase produced a phase transformation to a close-packed structure on the irradiated surface [5, 6]. Similar results were obtained in the β phase of a quaternary Cu–Zn–Al–Ni shape memory alloy [7]. No reports on the behavior of these alloys under swift heavy ion (SHI) irradiation exist in the literature.

When swift heavy ions penetrate into a solid, the main mechanism of energy deposition is electronic excitation and ionization. This high electronic energy deposition can generate cylindrical zones of modified matter surrounding the main ion trajectory, when the energy loss per unit length exceeds a threshold value [8]. Such defects, or tracks, form readily in electrical insulators but are not usually found in good electrical conductors [9]. The reason for such behavior is that a high concentration of conduction electrons can efficiently screen the space charge created by the incoming ions and rapidly spread the locally deposited energy. However, damage after SHI irradiation has been found in a few pure metals, like Fe, Ti and Zr, and in metallic compounds, typical examples of which are $NiZr_2$ and Ni_3B [9]. A common feature in these materials is that they are either easily amorphized or have various allotropic forms which can transform into each other.

In the shape memory intermetallic compound NiTi, a martensitic transformation exists between the cubic high temperature phase and the monoclinic low temperature phase. In this alloy, tracks have been observed after SHI irradiation of the monoclinic phase, but not when the irradiation was carried out in the cubic phase. The energy deposition threshold for track formation was 48 keV nm^{-1}. The tracks had an amorphous core and were surrounded by a region with cubic phase, that is, a region where the martensitic transformation temperature was reduced. At a lower rate of energy deposition, 32 keV nm^{-1}, no tracks were observed after irradiation in the martensitic phase, but the transformation from martensite to austenite was obtained after high irradiation fluences [10].

Based on the effects of SHI irradiation on Ni–Ti shape memory alloys, that include a martensite to austenite phase transformation due to the effects of energy deposition by electronic excitation and ionization, it was proposed to find out whether similar effects would be found in Cu based shape memory alloys. Therefore, in this work we explore the effects of SHI irradiation on the β phase and 18R martensitic phase of Cu based alloys.

2. Experimental details

Three different Cu based single crystals were prepared. The composition and corresponding martensitic start transformation temperatures (M_S) are shown in table 1.

All alloys were prepared using high purity Cu, Zn, Al and Ni metals. Alloys 1 and 2 were prepared by melting together the elements in sealed quartz tubes with Ar gas in an electrical furnace. To prepare alloy 3, a master Cu–Ni alloy was first obtained by vacuum arc melting in an Ar gas atmosphere. The homogeneity of the resulting button, after several remeltings, was verified by energy dispersive x-ray spectroscopy in a Philips 515 scanning electron microscope. The ternary alloy was then prepared by melting together the Cu–Ni alloy with the Al in a sealed quartz tube with Ar gas in an electrical furnace.

β-phase single crystals of the three alloys were grown by the Bridgman technique and homogenized for two days at 1070 K. Slices of nearly 5 mm diameter and 1 mm thickness from the single crystal grown from alloy 1 were cut with the surface normal close to $[001]_\beta$. In alloys 2 and 3, which are in the martensitic phase at room temperature, single variant crystals of the 18R structure were prepared by quenching the single crystal β phase from 1070 to 373 K (that is, above the M_s temperature) and stress inducing the martensitic transformation at 373 K, followed by cooling to room temperature under constant elongation. An Instron 5667 machine was used for this purpose. From the single variant 18R rods, oval shaped slices of approximately 6 mm × 8 mm × 1 mm with surface normal close to the $[210]_{18R}$ direction were cut using a low speed diamond wheel saw. Single crystal orientation was carried out with the Laue x-ray method.

One surface of each disc was prepared for irradiation by electropolishing using only one jet in a TENUPOL double jet apparatus. Samples of the three alloys were irradiated at room temperature using the ion accelerator at Ionenstrahllabor ISL of the Hahn-Meitner-Institut in Berlin, Germany. Details of each irradiation experiment are given in table 2.

Table 1. Composition and martensitic transformation temperature of the alloys studied under SHI irradiation.

Alloy	Composition	Transformation temperature, M_S (K)
1	Cu–22.7 at.%Zn–12.7 at.%Al	67 [10]
2	Cu–12.17 at.%Zn–17.92 at.%Al	335 [10]
3	Cu–27.25 at.%Al–2.16 at.%Ni	300 [10]

The energy deposition rate and the implantation range for all irradiation conditions reported in table 2 were calculated using the TRIM code [11]. After irradiation, the irradiated surfaces were protected with a thin layer of lacquer. From each irradiated specimen two samples of 3 mm diameter were obtained by sparked erosion. These samples were mechanically ground to a thickness of 0.2 mm from the unirradiated surface. Further thinning for TEM observation was carried out by electropolishing using only one jet in a TENUPOL double jet apparatus. The lacquer was then removed in an acetone bath and rinsed with ethanol. To compare the microstructure of irradiated and non-irradiated alloys, a reference specimen was also prepared from each alloy. All the specimens followed the same preparation procedures but the reference ones were not irradiated.

TEM characterization was carried out using a Philips CM200UT microscope, operated at 200 kV.

3. Results

3.1. SHI irradiation of the β phase

Figures 1(a) and (b) show the difference between the diffraction patterns of an unirradiated sample of Cu–Zn–Al and sample number 1 (table 2). Additional reflections can be seen in the pattern of the irradiated specimen, on streaks parallel to the $[1\ 1\ 0]_\beta$ and $[1\ \bar{1}\ 0]_\beta$ matrix directions, for example those indicated as C and D in figure 1(b). The additional reflections in figure 1(b) are similar to those reported in references [6, 7, 12]. They can be indexed as two perpendicular variants of a close-packed hexagonal structure with basal planes perpendicular to each other and parallel to the $(1\ 1\ 0)_\beta$ and $(1\ \bar{1}\ 0)_\beta$ matrix planes [12]. Figures 1(c) and (d) are dark field images obtained from the additional reflections (C and D, respectively) indicated in figure 1(b). Reflections C and D correspond to different variants of the close-packed phase. The regions that contribute to each reflection have an irregular shape and are complementary to each other in space. Within these regions, fine striations can be observed, indicating a large density of stacking faults.

3.2. SHI irradiation of the 18R martensitic phase

No differences between the diffraction patterns of unirradiated samples and samples irradiated with swift heavy ions were observed (figure 2(a)). No extra spots due to austenite, other martensite structure or gamma structure were detected. However, bright field images along the $[210]_{18R}$ zone axis of

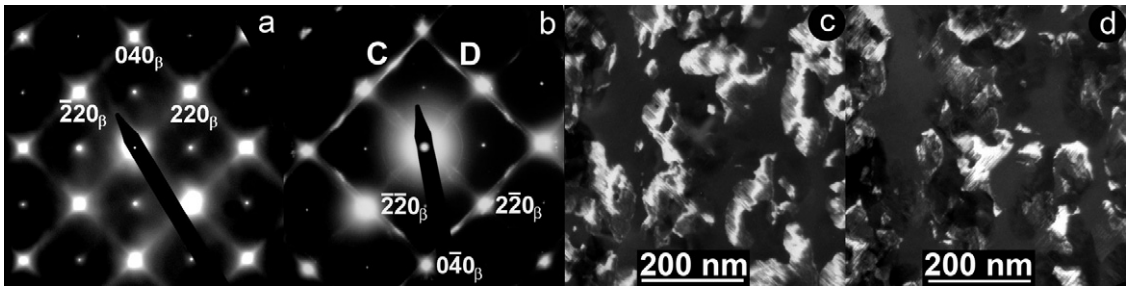

Figure 1. (a) Diffraction pattern of an unirradiated Cu–Zn–Al sample along $[001]_\beta$. (b) Diffraction pattern of sample 1 irradiated with 600 MeV of Au^+, along $[001]_\beta$. Additional reflections due to the formation of closed-packed phases can be observed. (c), (d) Dark field images taken with extra spots C and D, respectively.

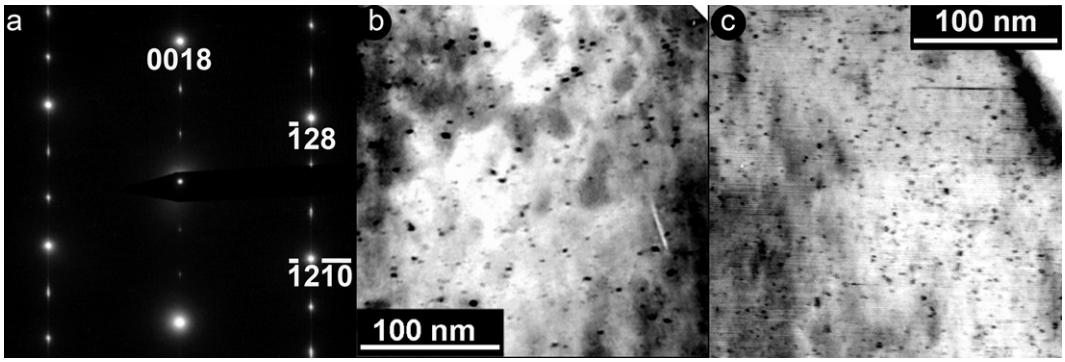

Figure 2. (a) Selected area diffraction pattern of a Cu–Zn–Al sample irradiated with 350 MeV Au^+, along the $[210]_{18R}$ zone axis (sample 7; fluence 5×10^{13} cm^{-2}). (b) Bright field image of the same sample obtained near the $[210]_{18R}$ zone axis. (c) Bright field image of a Cu–Al–Ni sample irradiated with 230 MeV Xe^+ obtained near the $[210]_{18R}$ zone axis (sample 4; fluence 1×10^{14} cm^{-2}). Nanometer size defects can be observed bright field electron micrographs in both (b) and (c).

Table 2. Main characteristics of swift heavy ion irradiation experiments carried out in this work: ion beam orientation, ion type, ion energy, energy deposition rate, fluence and implantation range.

Sample	Alloy	Ion beam orientation	Ion type	Energy (MeV)	Energy deposition rate (keV nm^{-1})	Fluence (cm^{-2})	Implantation range (μm)
1	1	$\sim[001]_\beta$	Au	600	52	1×10^{13}	18
2	2	$\sim[210]_{18R}$	Kr	200	23	7×10^{13}	13
3	2	$\sim[210]_{18R}$	Xe	230	39	1×10^{14}	11
4	3	$\sim[210]_{18R}$	Xe	230	39	1×10^{14}	11
5	2	$\sim[210]_{18R}$	Au	350	48	1×10^{12}	14
6	2	$\sim[210]_{18R}$	Au	350	48	1×10^{13}	14
7	2	$\sim[210]_{18R}$	Au	350	48	5×10^{13}	14
8	2	$\sim[210]_{18R}$	Au	600	52	1×10^{11}	19
9	2	$25°[210]_{18R}$	Au	600	52	5×10^{13}	18
10	2	$45°[210]_{18R}$	Au	600	52	5×10^{13}	18

the irradiated samples showed a high density of nanometer scale defects, shown in figures 2(b) and (c). The same kind of defects were detected in sample 7 of Cu–Zn–Al and in sample 4 of Cu–Al–Ni irradiated according to the fluence specified in table 2.

Figure 3 shows three micrographs of the same area of the irradiated specimen 2 (table 2) obtained in two beam diffraction conditions with different reflections from the $[210]_{18R}$ zone axis. The defects show a clear contrast in two beam conditions with $g = \bar{1}\ 2\ 8$ and $g = \bar{1}\ 2\ \bar{1}\bar{0}$, while they show no contrast with $g = 0\ 0\ 18$. This result implies that no elastic deformation was produced perpendicular to the basal planes.

In order to study the microstructure in the region a few micrometers below the irradiated surface, a thickness of about 5 μm was removed by electropolishing from the irradiated surface before thinning to electron transparency from the unirradiated side. In these samples, the same kinds of defect were observed as in the regions next to the irradiated surface, with similar size and number density per unit area.

The shape of the defects was independent of the energy deposition rate and fluence. The mean size of the projected

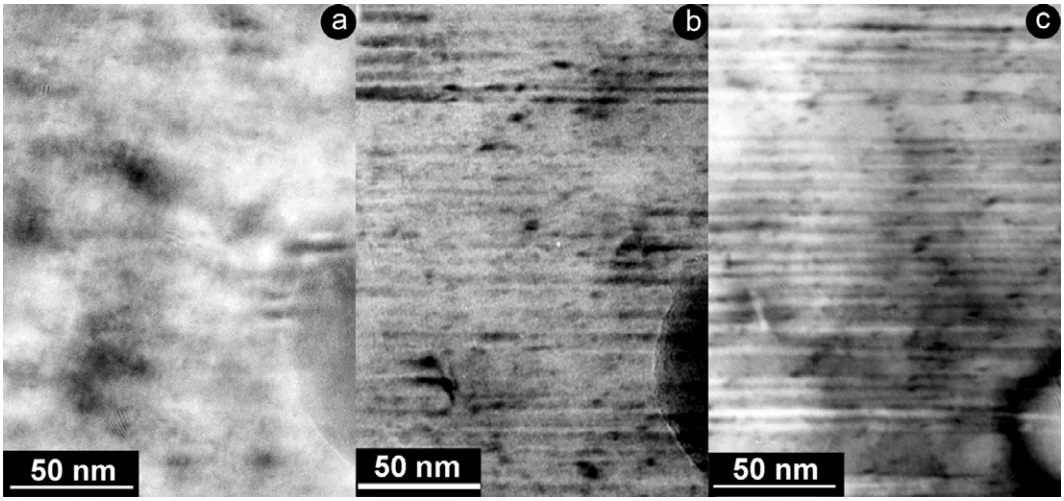

Figure 3. Bright field electron micrographs obtained in two beam conditions with (a) $g = 0\,0\,18$, (b) $g = \bar{1}\,2\,8$ and (c) $g = \bar{1}\,2\,\bar{1}\bar{0}$. The three images belong to the same area of a Cu–Zn–Al irradiated sample with 230 MeV of Xe+ (sample 3; fluence 1.10^{14} cm^{-2}).

Table 3. Mean density of defects per unit area for the swift heavy ion irradiations performed in 18R-Cu–Zn–Al samples.

Ion	Energy (MeV)	Fluence (cm^{-2})	Mean density of defects per unit area $\times 10^{11}$ (cm^{-2})
Kr	200	1×10^{13}	4.8
Xe	230	1×10^{14}	6.1
Au	350	1×10^{13}	3.7
Au	350	5×10^{13}	4.9
Au	600	1×10^{11}	3.1

shape of the defects along the $[210]_{18R}$ direction was (1.9 ± 0.4) nm parallel to the $[001]_{18R}$ direction and (3.4 ± 0.5) nm in the perpendicular direction.

The specimen was tilted in the microscope to investigate whether the defects had track morphology. No change in the defect morphology was found upon tilting. Due to the limited tilt allowed by the UT pole piece, the morphology of the defects was further investigated in irradiation experiments with the ion beam inclined to the specimen surface. Angles of inclination of 25° and 45° were used. In these experiments, the same morphology of the defects was observed as in the normal incidence experiments. This confirmed that the defects did not show a continuous contrast, but were equiaxed.

The number density of defects per unit area was found to be independent of the local thickness of the foil. Table 3 shows the mean number density of defects per unit area for several irradiation experiments. No correlation between defect density and fluence could be directly obtained from these results. In addition, a low fluence experiment (10^9 cm^{-2}) with a beam of 600 MeV gold ions was carried out. In this experiment almost no defects were identified and reliable estimates of defect density were not possible. A bright field image of this sample is shown in figure 4. Only basal faults can be distinguished in the micrograph.

Figure 5(a) shows a high resolution image of the defects obtained along the $[210]_{18R}$ zone axis of irradiated sample

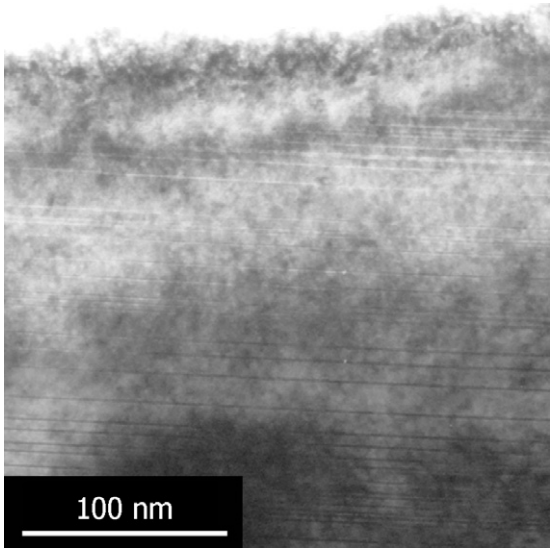

Figure 4. Bright field image of a Cu–Zn–Al sample irradiated with 600 MeV Au^+ and a fluence of 1×10^9 cm^{-2}, along the $[210]_{18R}$ zone axis.

number 3. The defects show facets parallel to the basal plane. A characteristic variation of the intensity from bright to dark can be observed when crossing the defects perpendicular to the basal planes from top to bottom. Within the defects, the basal planes could be distinguished, and no stacking faults were found. An enlarged image of one of the defects is shown in figure 5(b).

Figure 6 shows a HRTEM micrograph of the same region of sample 3 obtained along the $[210]_{18R}$ zone axis with different defocus values. This figure clearly illustrates that some defects are invisible at certain defocus values. In the matrix, it can also be noticed that for every three basal planes (vertical in these figures) one is brighter. This intensity modulation is due to a very slight inclination of the electron beam with respect to the $[210]_{18R}$ zone axis [13].

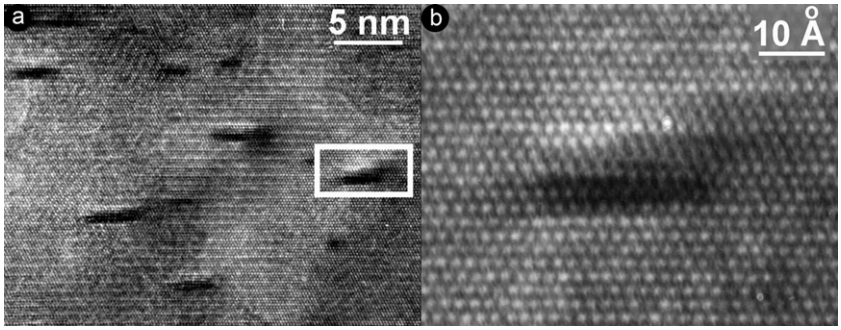

Figure 5. High resolution images of a Cu–Zn–Al irradiated sample with 230 MeV of Xe^{+} along $[210]_{18R}$ zone axis (sample 3; fluence 1×10^{14} cm^{-2}). (b) Enlarged image of the framed area in (a).

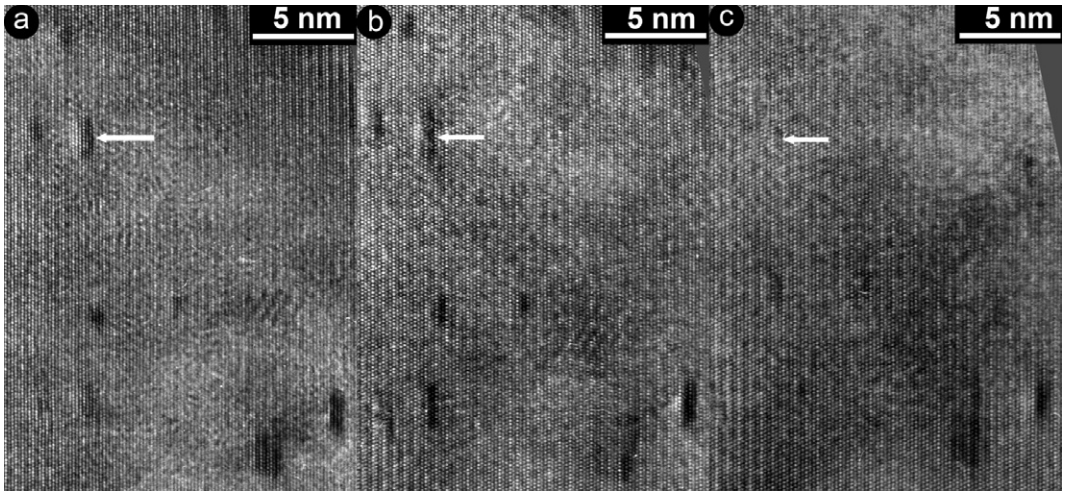

Figure 6. HRTEM images of a Cu–Zn–Al irradiated sample with 230 MeV of Xe^{+} along $[210]_{18R}$ zone axis with different defocus values: (a) defocus 33 nm; (b) defocus 51 nm; (c) defocus 55 nm. The arrow points to the same area in the three micrographs. Basal planes are vertical in these figures.

4. Discussion

A marked difference between the response of the β phase and the 18R martensitic phase to SHI irradiation was observed. Over the surface of the irradiated β phase, a phase transformation to a close-packed phase was found. No further defects were observed in the bulk. Instead, in the 18R martensite the effect of SHI irradiation was to introduce nanometer sized defects without any major change of the crystal structure. In the Cu–Zn–Al and Cu–Al–Ni martensites no transformation to austenite was observed, even after high fluences with high energy deposition rates. These effects contrast with those observed in Ni–Ti shape memory alloys, where no effects were observed in the austenite phase in Ni–Ti after SHI irradiation, while in the martensitic phase, amorphous tracks were observed when the deposition rate was above 48 keV nm^{-1}. The region surrounding the amorphous tracks was transformed to the austenite phase [9]. After high fluence irradiations, the martensite completely transformed to austenite and amorphous phases. The result that no tracks were observed in the Cu based martensites is probably related to the fact that Cu based alloys are not amorphized, and therefore agrees with the general trend that track formation by SHI irradiation occurs more readily in materials that are easily amorphized by elastic collisions than in those which are not [10].

The effects of SHI irradiation on the microstructure of the β phase $[001]_{\beta}$ Cu–Zn–Al samples are similar to those observed under lower energy, cascade producing ion irradiations (170–300 keV Cu or 30 keV Ar), in which a 2H close-packed structure with two interpenetrated variants was induced [12]. However, the transformation to a close-packed phase under SHI irradiation (1×10^{13} ion cm^{-2}) was observed after lower fluences than under lower energy ion irradiations, where effects were observed only after 2×10^{14} ion cm^{-2} in $[001]_{\beta}$ Cu–Zn–Al samples and 5×10^{13} ion cm^{-2} in $[110]_{\beta}$ Cu–Zn–Al samples [5, 6].

In the 18R martensitic phase, no phase transformation was observed due to SHI irradiation even at the highest fluences, in contrast to what was observed in NiTi martensites. Instead, a high density of nanometer sized defects was observed in all 18R irradiated samples. Similar defect densities were observed in areas close to the irradiated surface and at a depth of about 5 μm from the irradiated surface. This result shows that the formation of defects is not restricted to regions close to the irradiated surface, but also takes place in bulk regions within the penetration range of the ions. The defects were observed in both Cu–Zn–Al and Cu–Al–Ni, indicating that

their formation does not depend on the presence of Zn or Ni in the alloy and is not very sensitive to the specific Al content, which varies between 18 and 27 at.% in both alloys. Defect formation was also insensitive to the species of bombarding ion and to energy deposition rates, ranging from 23 to 52 keV nm^{-1}. These sorts of defects were never detected under other types of irradiation [3] or thermal treatment [2]. Both kind of procedures reported only a stabilization (shift of transformation temperature) of the 18R martensite.

Although the plate morphology of the plates is similar to the γ_2 structure present in Cu–Al–Ni samples, the size of the defects reported here are two times smaller than the ones shown in [14]. Moreover, the gamma phase in Cu–Zn–Al does not present any morphology comparable to the defects reported here.

By tilting the irradiated specimens in the TEM and also with SHI irradiation experiments with an inclined angle of incidence with respect to the specimen surface within the range of $0° - 45°$, it was found that the defects did not have the morphology of tracks. Such morphology could be expected due to the high energy loss of the ions, and has been observed after SHI irradiation of Ni–Ti shape memory alloys [9]. Instead, the present results show that the defects were equiaxed. Alignment of defects parallel to the incident beam direction was not observed either.

The observed density of defects was approximately the same at different foil thicknesses. This suggests that the defects produce visible contrast only when located within a certain depth from the foil surface.

Strikingly, no dependence of the defect density per unit area was found with the ion fluence in the range of 10^{11}–10^{14} ions cm^{-2} (table 3). Below the lower fluence, very few defects could be observed, and no reliable defect density could be determined. This means that defect density rapidly reaches saturation. These observations can be rationalized by assuming that the defects result from the interaction of individual ions with the lattice, and that when an ion impacts on a previously damaged region, it erases the effects of the previous ions and creates new defects. This assumption is supported by the fact that the defects show a very small dispersion in size. Subsequent evolution of the defects after production due to further irradiation would be expected to show a larger dispersion in size, or a dependence of size and morphology on fluence. For the lowest fluence of 10^{11} cm^{-2}, the mean distance between incident ions is about 30 nm. Since the defects were randomly distributed, this implies that defects are created by the incident ions within an area with a radius of at least 15 nm. Lower fluence experiments performed to improve this estimate failed to produce a significant number of defects.

As discussed above, the nanoscale defects observed after SHI irradiation of 18R martensite are believed to be formed due to the effect of individual ions during their trajectory through the crystal. The main energy deposition mechanism is that of electronic excitations. Nevertheless, cascade forming collisions also occur. Therefore, one possibility for the structure of the defects is that they are vacancy clusters resulting from displacement cascade events.

In order to analyze this possibility, a detailed analysis of the output of TRIM simulations was carried out using the calculation methods performed in [15]. The total number of collisions that result in a primary knock-on atom (PKA) with energy larger than a certain energy E was calculated as a function of E. The results are shown in figure 7. Assuming cascades are produced by PKA with energies above 1 keV, it can be seen that the estimated number of cascades is of the order of 10/ion μm. Considering a cascade volume of 4×10^{-6} μm^3 and a fluence value of 10^{11} ion cm^{-2}, at which saturation of the number density of defects is observed, the overlapping fraction volume would be given by:

Overlap fraction volume $= 4000$ nm^3 (volume of a cascade) 0.01(cascades/ion nm) $\times$ 10^{-3} ions nm^{-2}(fluence) $=$ 0.04.

On the other hand, no heterogeneous distribution of defect density on the samples was observed. Moreover, the density of defects is constant for different values of fluence. Therefore, there is no possibility of understanding the creation of defects by collisional effects alone with an overlapping fraction volume lower than one.

The other major effect of the high energy ions is the production of a thermal spike. The temperature distribution around the ion trajectory has been estimated by calculations and computer simulations. According to [16], temperatures near that of the melting point can be reached. Computer simulations indicate that local melting can occur. During the thermal spike evolution, very high temperature gradients are formed, that can induce local segregation by thermomigration. Due to the short time elapsing during the irradiation process (between 1 and 100 ps) no local thermodynamic equilibrium can be expected in the segregation obtained. Simulations of SHI irradiation in Au–Ni using molecular dynamics have shown that Ni atoms have the tendency to migrate towards the hot core of the thermal spike, leading to composition fluctuations in the zone affected by the thermal spike [17]. Therefore, the observed defects in the present experiments could be the result of local composition modulations caused by thermomigration during the spike event.

In order to characterize the structure of the defects, their contrast in high resolution TEM images was compared to that

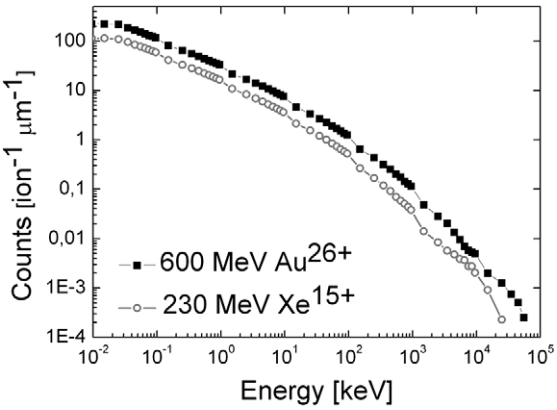

Figure 7. Calculated number of collisions that result in a primary knock-on atom (PKA) with energy larger than a certain energy E, as function of E, obtained from the output of TRIM simulations. The target used for the calculation was a 20 μm thick, Cu–12.17 at.%Zn–17.92 at%.Al foil.

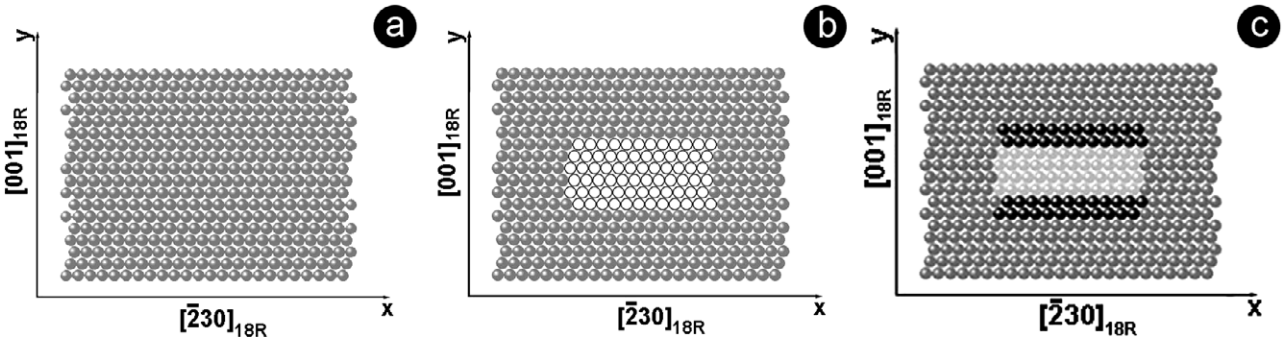

Figure 8. Schematic drawings of the defects in the 18R structures used as input for contrast simulation. (a) Distribution of the atomic columns in the first and third slices. (b) Distribution of the atomic columns in the second slice for the vacancy model and the atomic cluster model. (c) Distribution of the atomic columns in the second slice for the local segregation model.

of simulations assuming different defect types. These results will be shown next.

4.1. Image simulation of the nanometric defects in the 18R martensitic phase

Based on the above discussion, different types of defects were assumed and the contrast they would produce in HRTEM images was simulated. The matrix composition was taken as that of the Cu–Zn–Al (alloy 2) martensite, since most of the experiments were carried out in this alloy. The first type of defect proposed was a cluster of vacancies within a perfect 18R structure. The second type of defect was a cluster of pure Cu, Zn or Al with the 18R structure surrounded by a perfect Cu–Zn–Al 18R structure. The third defect was a local segregation of Cu and Al atoms perpendicular to the basal planes, namely, a region enriched in Al atoms (Cu depleted) in between Al depleted zones (Cu rich). For the latter case, a composition modulation involving only Cu and Al was assumed, since the defects were observed in both the Cu–Zn–Al and the Cu–Al Ni martensites, suggesting that neither Zn nor Ni were essential for their formation.

In order to simulate the contrast of these defects, a supercell was constructed consisting of three slices perpendicular to the $[210]_{18R}$ direction. Each slice had a length of 24 atomic columns along the $[230]_{18R}$ direction and a width of 18 basal planes, which means a total of 432 atomic columns occupying the normal positions of the 18R structure. The distribution of the atomic columns from the $[210]_{18R}$ direction is shown in figure 8(a), where the **x**-axis corresponds to $[230]_{18R}$, the **y**-axis corresponds to $[001]_{18R}$ and the **z**-axis corresponds to $[210]_{18R}$. The columns of the first and third slices were composed of n atoms along $[210]_{18R}$ with an occupation probability obtained from the composition of the Cu–Zn–Al alloy. The columns of the middle slice had m atoms. The total thickness of the supercell was $D = (2n + m)^{*}d$, where d is the distance between atoms along $[210]_{18R}$. From the lattice parameters in reference [17] $d = 0.259$ nm is obtained. By changing n and m the total thickness of the supercell and the ratio of the middle slice thickness to that of the first or third slice (m/n) could be varied. The different defect types were constructed by modifying the composition of the middle slice.

To simulate the vacancy cluster, six rows along $[230]_{18R}$, each 12 atomic columns in length, were removed from the middle slice leaving vacant sites (figure 8(b)). To simulate clusters of pure Cu, Zn or Al atoms, the vacant sites in figure 8(b) were replaced by Cu, Zn or Al atoms. The composition modulation was built by replacing eight rows of the normal composition in the middle slice, each 12 atomic columns in length, by two rows of Cu atoms, followed by four rows enriched in Al, with a composition of 35.84 at.% Al–64.16 at.% Cu, and again two rows of Cu atoms (figure 8(c)).

In each case, the ratio of the middle slice thickness to that of the first or third slice (m/n) was varied between $m/n = 1$ and $m/n = 30$. The total thickness was varied between 0.777 and 20.7 nm, and the defocus value was varied between 20 and 60 nm. In order to reproduce the modulation of the intensity of the basal planes in the matrix surrounding the defects that was observed in the experimental images, a slight inclination of the electron beam with respect to the $[210]_{18R}$ zone axis was introduced. This inclination also had an effect on the contrast of the defects.

4.2. Simulation results

(*a*) *Vacancy model*. With this model, the simulated images could not reproduce the contrast observed in the experimental images. The contrast from the vacancy region was too weak.
(*b*) *Atomic cluster model*. The simulations of a cluster of Cu or Zn atoms showed intensity variations between the defect and the matrix, but the details observed in the experimental images could not be correctly reproduced.
(*c*) *Local segregation model*. With this model, good agreement between simulated and experimental images was obtained. The parameters used for the simulation that showed the best agreement were $D = 9.3$ nm, $m/n = 30$, a defocus of 20 nm and a tilt of the incident beam of 0.25° (figure 9(a)). In this figure not only is a change of intensity in the central zone of the defect observed, but also the characteristic bright–dark contrast observed in figure 4 could be reproduced. In figure 8(b) a simulated image with the values and the model used in figure 9(a) but no tilt of the incident beam was included. This simulation indicates that the intensity modulation observed in the HRTEM images of the defects is related to a slight inclination of the electron beam with respect to the zone axis. Figure 9(c) shows how the contrast of the defect is strongly reduced at specific defocus values, in agreement with the results described in figure 6.

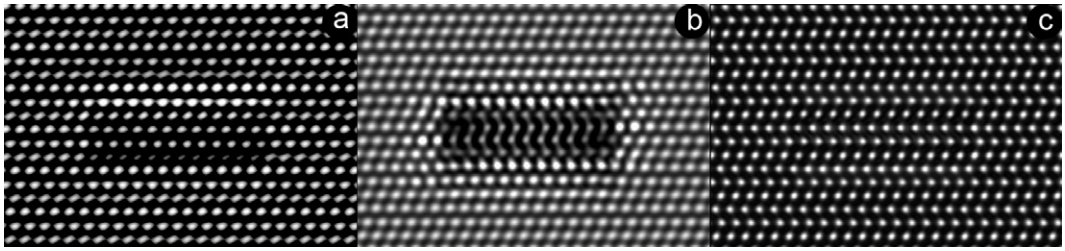

Figure 9. High resolution image simulations of a defect corresponding to the local segregation model. (a) Defocus = 20 nm, total thickness = 9.3 nm and beam tilt 0.25°. (b) Defocus = 20 nm, total thickness = 9.3 nm and no tilt. (c) Defocus = 45 nm, total thickness = 9.3 nm and tilt 0.25°.

Summarizing the results of this section, qualitative agreement between images and simulations was obtained by assuming the defects to consist of a local composition modulation with no change in structure. These modulations could be caused by thermomigration induced by the very large temperature gradients during the thermal spike event. Such composition modulations have also been obtained by computer simulation of thermal spikes in Au–Ni alloys [18].

5. Conclusions

The behavior of Cu based shape memory alloys under SHI irradiation was studied in this paper. A phase transformation to a close-packed structure on the irradiated surface was observed in the austenite phase. In contrast, the 18R phase shows a higher stability under irradiation. This behavior is just the opposite to that observed in Ti–Ni shape memory alloys, where no defects were detected in the austenite. No change in structure was caused even after very high fluences. Nanometer scale defects were observed that are probably the result of collisional effects and local composition modulations caused by thermomigration during the thermal spike event.

Acknowledgment

Dr M Alurralde is gratefully acknowledged for his help with the analysis of the output of the TRIM simulations.

References

[1] Ahlers M 1974 *Scr. Metall.* **8** 213
[2] Ahlers M 1986 *Prog. Mater. Sci.* **30** 135
[3] Tolley A 1994 *Radiat. Eff. Defects Solids* **128** 229
[4] Tolley A 1995 *Phil. Mag.* A **72** 1633
[5] Tolley A and Abromeit C 1995 *Scr. Metall. Mater.* **32** 925
[6] Zelaya E, Tolley A, Condo A M, Fichtner P F P and Bozzano P B 2005 *Scr. Mater.* **53** 109
[7] Zelaya E, Tolley A, Condó A M and Fichtner P F P 2007 *Mater. Sci. Eng.* A **444** 178
[8] Seitz F and Koehler J S 1956 *Solid State Phys.* **305** 2
[9] Barbu A, Dammak H, Dunlop A and Lesueur D 1995 *MRS Bull.* **20** 29
[10] Barbu A, Dunlop A, Hardouin Duparc A, Jaskierowicz G and Lorenzelli N 1998 *Nucl. Instrum. Methods Phys. Res.* B **145** 354
[11] Biersack J P and Haggmark L G 1980 *Nucl. Instrum. Methods* **174** 257
[12] Tolley A and Sánchez E A 2002 *Lat. Am. Appl. Res.* **32** 317
[13] Coene W, Bender H, Lovey F C, Van Dyck D and Amelinckx S 1985 *Phys. Status Solidi* **87** 483
[14] Zarubova N, Gemperle A and Novak V 1997 *Mater. Sci. Eng.* A **222** 166
[15] Paschoud F, Alurralde M, Szenes G, Havancsak K and Victoria M 1993 *Radiat. Eff. Defects Solids* **126** 177
[16] Toulemonde M, Dufour Ch, Wang Z and Paumier E 1996 *Nucl. Instrum. Methods* B **112** 26
[17] Guenin G, Pynn R, Rios Jará D, Delaey L and Gobin F P 1980 *Phys. Status Solidi* a **59** 553
[18] Lopasso E, Caro M and Caro A 2001 *Phys. Rev.* B **63** 174105